



Engineering of a NIR-activable hydrogel-coated mesoporous bioactive glass scaffold with dual-mode parathyroid hormone derivative release property for angiogenesis and bone regeneration

Shi Liu^{a,1}, Zhengzhe Han^{b,1}, Ji-Na Hao^a, Dapeng Zhang^a, Xianglong Li^a, Yuanyuan Cao^a, Jinghuan Huang^{b,**}, Yongsheng Li^{a,c,*}

^a Lab of Low-Dimensional Materials Chemistry, Key Laboratory for Ultrafine Materials of Ministry of Education, Frontier Science Center of the Materials Biology and Dynamic Chemistry, Shanghai Engineering Research Center of Hierarchical Nanomaterials, School of Materials Science and Engineering, East China University of Science and Technology, Shanghai, 200237, China

^b Department of Orthopedic Surgery and Shanghai Institute of Microsurgery on Extremities, Shanghai Jiao Tong University Affiliated Sixth People's Hospital, 600 Yishan Road, Shanghai, 200233, PR China

^c Key Laboratory for Green Processing of Chemical Engineering of Xinjiang Bingtuan, School of Chemistry and Chemical Engineering, Shihezi University, Shihezi, 832003, China

ARTICLE INFO

Keywords:

Parathyroid hormone
Dual-mode release
Thermosensitive hydrogel
Angiogenesis
Bone regeneration

ABSTRACT

Osteogenesis, osteoclastogenesis, and angiogenesis play crucial roles in bone regeneration. Parathyroid hormone (PTH), an FDA-approved drug with pro-osteogenic, pro-osteoclastogenic and proangiogenic capabilities, has been employed for clinical osteoporosis treatment through systemic intermittent administration. However, the successful application of PTH for local bone defect repair generally requires the incorporation and delivery by appropriate carriers. Though several scaffolds have been developed to deliver PTH, they suffer from the weaknesses such as uncontrollable PTH release, insufficient porous structure and low mechanical strength. Herein, a novel kind of NIR-activable scaffold (CBP/MBGS/PTHrP-2) with dual-mode PTHrP-2 (a PTH derivative) release capability is developed to synergistically promote osteogenesis and angiogenesis for high-efficacy bone regeneration, which is fabricated by integrating the PTHrP-2-loaded hierarchically mesoporous bioactive glass (MBG) into the N-hydroxymethylacrylamide-modified, photothermal agent-doped, poly(N-isopropylacrylamide)-based thermosensitive hydrogels through assembly process. Upon on/off NIR irradiation, the thermoresponsive hydrogel gating undergoes a reversible phase transition to allow the precise control of on-demand pulsatile and long-term slow release of PTHrP-2 from MBG mesopores. Such NIR-activated dual-mode delivery of PTHrP-2 by this scaffold enables a well-maintained PTHrP-2 concentration at the bone defect sites to continually stimulate vascularization and promote osteoblasts to facilitate and accelerate bone remodeling. *In vivo* experiments confirm the significant improvement of bone reparative effect on critical-size femoral defects of rats. This work paves an avenue for the development of novel dual-mode delivery systems for effective bone regeneration.

1. Introduction

High-efficacy treatment of bone defects, especially large bone defects caused by tumor resection, infection, trauma, or aging remains a major

challenge in clinical orthopedics [1–3]. Currently, the clinically traditional approaches for bone tissue repair mainly include autologous and allogeneic bone grafting, however, they are greatly limited by the donor shortage and insurmountable immune rejection, respectively [4–7]. To

Peer review under responsibility of KeAi Communications Co., Ltd.

* Corresponding author. Lab of Low-Dimensional Materials Chemistry, Key Laboratory for Ultrafine Materials of Ministry of Education, Frontier Science Center of the Materials Biology and Dynamic Chemistry, Shanghai Engineering Research Center of Hierarchical Nanomaterials, School of Materials Science and Engineering, East China University of Science and Technology, Shanghai, 200237, China.

** Corresponding author.

E-mail addresses: huangjh931@163.com (J. Huang), ysli@ecust.edu.cn (Y. Li).

¹ These authors contributed equally to this work.

<https://doi.org/10.1016/j.bioactmat.2023.02.008>

Received 11 October 2022; Received in revised form 6 February 2023; Accepted 8 February 2023

Available online 20 February 2023

2452-199X/© 2023 The Authors. Publishing services by Elsevier B.V. on behalf of KeAi Communications Co. Ltd. This is an open access article under the CC BY-NC-ND license (<http://creativecommons.org/licenses/by-nc-nd/4.0/>).

overcome these limitations, bone tissue engineering, which combines biomaterial-based scaffolds incorporated with bone repair agents has been emerging as a promising tool for the treatment of critical-sized bone defects [1,8–10].

Numerous vital functions are regulated by pulsed or intermittent release of bioactive molecules at a specific times and locations as is found in the living organisms. Many kinds of new bioactive proteins and peptides have been produced as novel therapeutic drugs in genetic engineering. Brabant et al. [11] reported a series of endogenously released hormones in a pulsatile manner. Research with hormones such as growth hormones [12], gonadotropin-releasing hormone (GnRH) [13], parathyroid hormone (PTH) [14], and insulin shows that optimal therapeutic effects come from periodically fluctuating drug concentrations. PTH belongs to another group of compounds with pulsatile release characteristics regulated by changes of extracellular serum ionized calcium mediated by calcium-sensing receptor (CaSR) on parathyroid cells. As an ideal candidate for bone repair agents, PTH exhibits the ability to activate both osteoblasts and osteoclasts and promote angiogenesis. It has been approved by the U.S. Food and Drug Administration (FDA) to treat osteoporosis through systemic intermittent administration in clinical therapy [15–17]. Although the systemic intermittent administration of PTH, unlike the continuous systemic administration that predominantly increases osteoclast activity and leads to bone resorption, shows a higher activation effect on osteoblasts than osteoclasts and promotes bone volume accumulation for osteoporosis therapy [18–20], it is hardly applied to local bone defect repair owing to either the poor therapy efficiency caused by the low drug concentration delivered to the bone sites or the adverse side effects resulting from a higher dose of injection [21,22]. A novel PTH-related peptide (PTHrP-2: S^[PO4]VSEI-QLMHN-LGKHL-NSMER-VEWLR-KKLQD-VHNF-EEE) is easier to synthesize in large quantities at a lower cost compared with pure PTH [23]. A phosphorylated Ser at the N-terminus and a triple Glu motif at the C-terminus of PTHrP-2 are the key differences between PTHrP-2 and PTH. Studies have shown that several proteins with the sequence of an acidic amino acid (Glu) in their structure as calcium-binding sites could bind calcium-based materials firmly [24,25], which could increase the induction of osteogenic capacity through the exposure of peptide active sites after binding to calcium-containing materials and the controlled release characteristics. To address these issues and extend the PTH or its derivative application from systemic osteoporosis treatment to localized bone regeneration, a pulsatile PTH delivery scaffold based on hydrogel was developed recently to simulate intermittent PTH injection [26]. However, its disconnected micropores affect the recruitment and proliferation of osteogenic cells, and could not provide adequate spaces for vascularization and new bone formation. Besides, the inherently low mechanical strength and LCST (lower critical dissolution temperature) as well as the fast degradation of the utilized hydrogel limits its performance in bone repair applications. Another scaffold based on MBG with an interconnected porous structure and good mechanical strength was employed to load the PTH derivative for bone defect repair [23]. Unfortunately, it is difficult to precisely control the drug release through the MBG degradation, which is inevitably affected by the microenvironment *in vivo*. Near-infrared (NIR) light has been reported to be suitable for biological application as it exhibits remarkable deep tissue penetration ability with minimum damage to biological specimens and living tissues [27–29]. In a noninvasive manner, NIR light can provide near-instantaneous therapy with precise spatiotemporal control *in vitro*. Hence, it is highly desirable to develop a NIR stimuli-responsive drug delivery system with a suitable porous structure, excellent bioactivity and mechanical property to realize the precisely controlled release of PTH in sustained and pulsatile release manners.

Motivated by these investigations, we preconceived that decorating the PTHrP-2-loaded MBG with a stimuli-responsive hydrogel shell with suitable LCST as a “gating” to control the opening of its macro- and mesopores would be an effective strategy for the spatiotemporal control of PTHrP-2 release. Nevertheless, such a delivery system for PTHrP-2

has not yet been developed so far. Herein, a thermosensitive hydrogel-coated MBG-based scaffold (CBP/MBGS) was fabricated to deliver the PTHrP-2 and achieve its dual-mode (sustained and pulsatile) controlled release for promoted angiogenesis and high-efficacy bone regeneration (Fig. 1). Specifically, the thermally responsive hydrogel with enhanced LCST above body temperature was first designed and synthesized by copolymerization of monomeric N-isopropylacrylamide (NIPAm) and hydrophilic N-hydroxymethylacrylamide (NMA). Incorporation of carbon dots (CDs)-doped bioglass nanoparticles (CDBGn) as a photothermal converter into the polymer hydrogel during polymerization afforded the CDBGn-doped, NMA-modified PNIPAm hydrogels (denoted as CDBGn/P (NIPAm-co-NMA) with suitable LCST and NIR responsiveness. Subsequently, the PTHrP-2-loaded hierarchical MBG was integrated into the CDBGn/P(NIPAm-co-NMA) hydrogel matrix during the assembly to construct the thermosensitive hydrogel-coated MBG scaffold (MBGS) with PTHrP-2 in its mesopores, designated as CBP/MBGS/PTHrP-2 (Fig. 1A). After implanting the CBP/MBGS/PTHrP-2 into the bone defect site, thermosensitive hydrogel shell undergoes reversible phase transitions upon on/off NIR-laser irradiation, enabling it to serve as a “gating” to accurately control the sustained and pulsatile release of PTHrP-2 by regulating the opening of MBG pores (Fig. 1B). Benefiting from such dual-mode release capability, the CBP/MBGS/PTHrP-2 exhibits strong osteogenic and proangiogenic effects on bone mesenchymal stem cells (BMSCs) and human umbilical vein endothelial cells (HUVECs), resulting in satisfactory angiogenic and bone reparative effects *in vitro* and *in vivo* (Fig. 1C). This work provides a new paradigm for the rational design and preparation of PTH derivative-loaded scaffold material for high-efficacy bone defect repair.

2. Results and discussion

2.1. Characterization and photothermal property of CDBGn/P(NIPAm-co-NMA) hydrogels

The CDBGn/P(NIPAm-co-NMA) hydrogels were fabricated by a one-pot polymerization of NIPAm and NMA with CDBGn dispersed homogeneously in the polymer framework, as illustrated in Fig. 1A. Initially, bioactive glass nanoparticles (BGn) were synthesized according to the method we reported previously [30,31]. CDs were then formed *in situ* on BGn by sintering 3-aminopropyltriethoxysilane (APTES) onto their surface, affording the CD-doped BGn (denoted as CDBGn). The as-prepared CDBGn exhibit a well-defined spherical morphology with an average diameter of 130 nm as well as uniform small mesopores of 2 nm and large mesopores of 10.9 nm throughout the nanoparticles (Fig. 2A and S1-2). It is observed that the CDBGn aqueous suspension emits bright blue light once irradiated by a 365 nm UV-light, with a broad emission band centered at 485 nm upon excitation at 380 nm (Fig. 2B), which is ascribed to the intrinsic fluorescence properties of CDs [32–34], demonstrating the successful formation of CDs on the BGn. To analyze the surface structure and composition of CDBGn, Raman spectra and X-ray photoelectron spectroscopy (XPS) analysis were carried out. Fig. S3A shows the characteristic Raman band of C sp³ and sp² at ~1450 and ~1600 cm⁻¹, respectively, suggesting the presence of disordered and graphitized structures in the CDBGn [35,36]. The wide-scan XPS spectrum of CDBGn confirms the coexistence of Si, Ca, C, N and O elements (Fig. S3B). The high-resolution C1s XPS spectrum (Figs. S3C and S3D) shows three fitting peaks at 284, 285 and 288 eV, attributed to C–C, C–N and C–O bonds, respectively. The N1s XPS spectrum presents the peaks of N–H (399.3 eV), (C)₃–N (400.4 eV) and C–N (397.6 eV), which indicates that nitrogen is mainly bound to carbon and forms different local energy states with distinct emission centers [37]. These results demonstrate the successful synthesis of CDBGn. Afterwards, the photothermal properties of the resultant CDBGn were investigated by measuring their time-dependent temperature variations at different concentrations under an 808 nm NIR laser irradiation (1 W/cm²). As revealed in Fig. 2C, the temperature increase shows a strong dependency

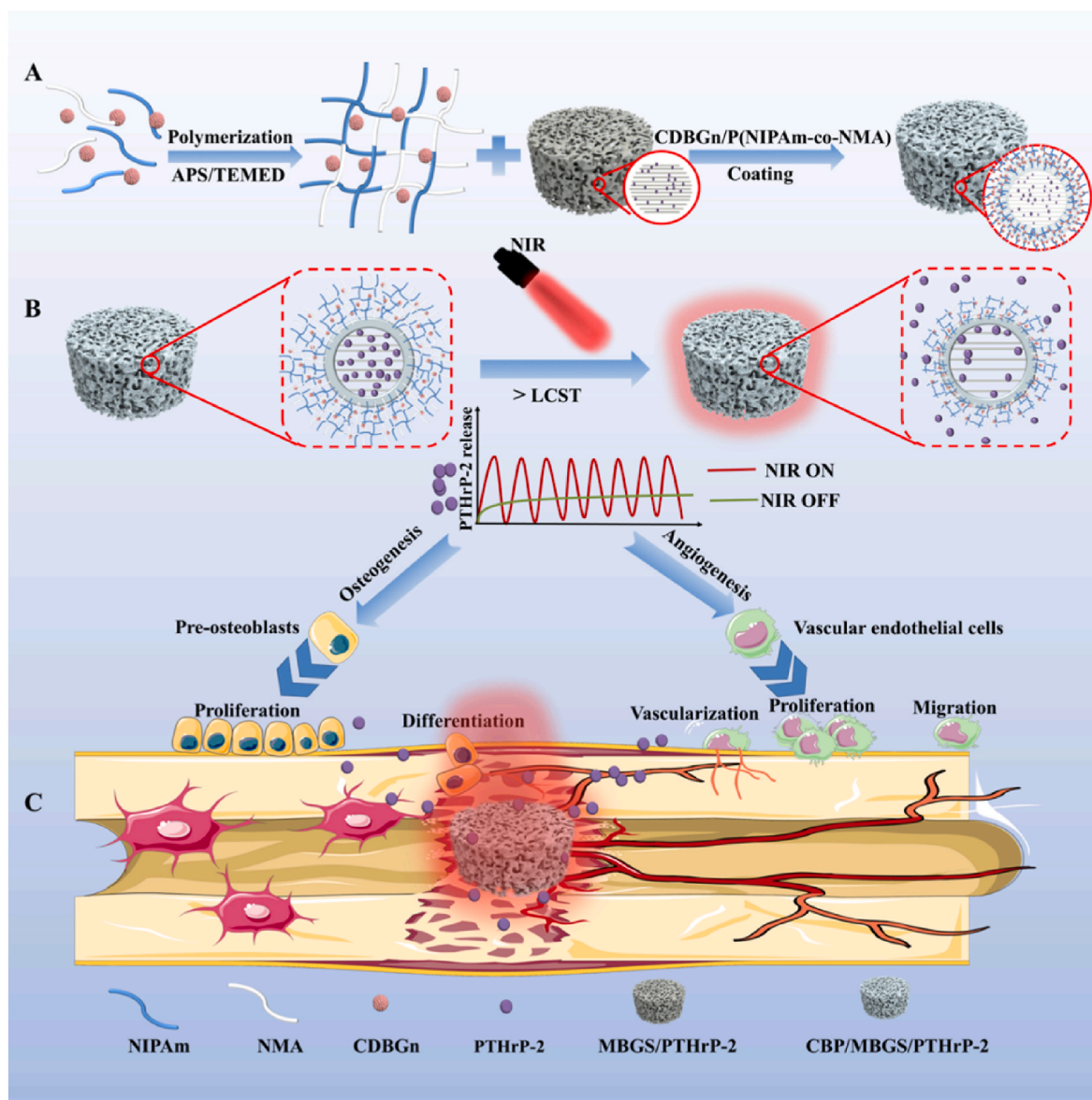


Fig. 1. Schematic diagram of the synthesis and mechanism of CBP/MBGS/PTHrP-2 bioscaffolds with functions of regulating angiogenesis and osteogenesis to promote bone regeneration.

on both irradiation time and CDBGn concentrations, and the temperature of CDBGn dispersion with the concentration of 100 and 400 $\mu\text{g}/\text{mL}$ is elevated to about 45 and 70 $^{\circ}\text{C}$ upon irradiation for 5 min, respectively, indicating that CDBGn displays good photothermal conversion performance.

Subsequently, as photothermal converters, the as-synthesized CDBGn were introduced into the thermosensitive P(NIPAm-co-NMA) hydrogel networks during the copolymerization of NIPAm and NMA to fabricate CDBGn/P(NIPAm-co-NMA) with NIR responsiveness. The LCST of PNIPAm homopolymer is about 32 $^{\circ}\text{C}$, which is not suitable for *in vivo* application [38,39] and needed to be enhanced to around body temperature (~ 40 $^{\circ}\text{C}$). Here, we employed the strategy of incorporating another hydrophilic NMA fragment in PNIPAm to adjust its LCST. In detail, hydrophilic monomer NMA [40,41] was copolymerized with NIPAm monomer in one-pot with different feeding ratios. Two P(NIPAm-co-NMA) copolymer hydrogels with different molar ratios of monomers added before the one-pot polymerization were prepared and tested for obtaining the optimal LCST. As shown in Fig. S4, the LCST of P(NIPAm-co-NMA) was elevated higher than 40 $^{\circ}\text{C}$, compared with that of PNIPAm homopolymer (32 $^{\circ}\text{C}$), when the molar ratio of NMA/NIPAm

monomers is 1:10 or 1:8, respectively. The increase of LCST can be attributed to the fact that the hydroxymethyl groups of NMA alter the hydrophilic/hydrophobic balance of the hydrogels [42,43]. Considering that the LCST of the copolymer hydrogel with a monomer ratio of 1:10 is closer to the body temperature and qualified for *in vivo* application, it was thus selected for the follow-up research. In addition, the hydrogel can undergo a rapid volume phase transition at the onset temperature (40.73 $^{\circ}\text{C}$) in DSC curve. Therefore, we decided to use the lowest possible temperature which still resulted in a consistent effect without compromising the results. The thermoresponsive phase transition behavior of P(NIPAm-co-NMA) hydrogel was recorded in Fig. S5, which shows that the hydrogel undergoes a sharp phase transformation from a swelling state to a shrunken state after heating at 41 $^{\circ}\text{C}$ for 30 s, suggesting its potential ability to control the drug release by temperature. Then, the P(NIPAm-co-NMA) hydrogel incorporated with CDBGn (100 $\mu\text{g}/\text{mL}$) was fabricated, and its photothermal stability was further investigated. As presented in Fig. 2E and F, the CDBGn/P(NIPAm-co-NMA) hydrogel displays a rapid temperature increase to 44 $^{\circ}\text{C}$ after laser irradiation (1 W/cm^2) for 5 min, and such heating efficiency is well maintained throughout five cycles of laser on/off irradiation, verifying

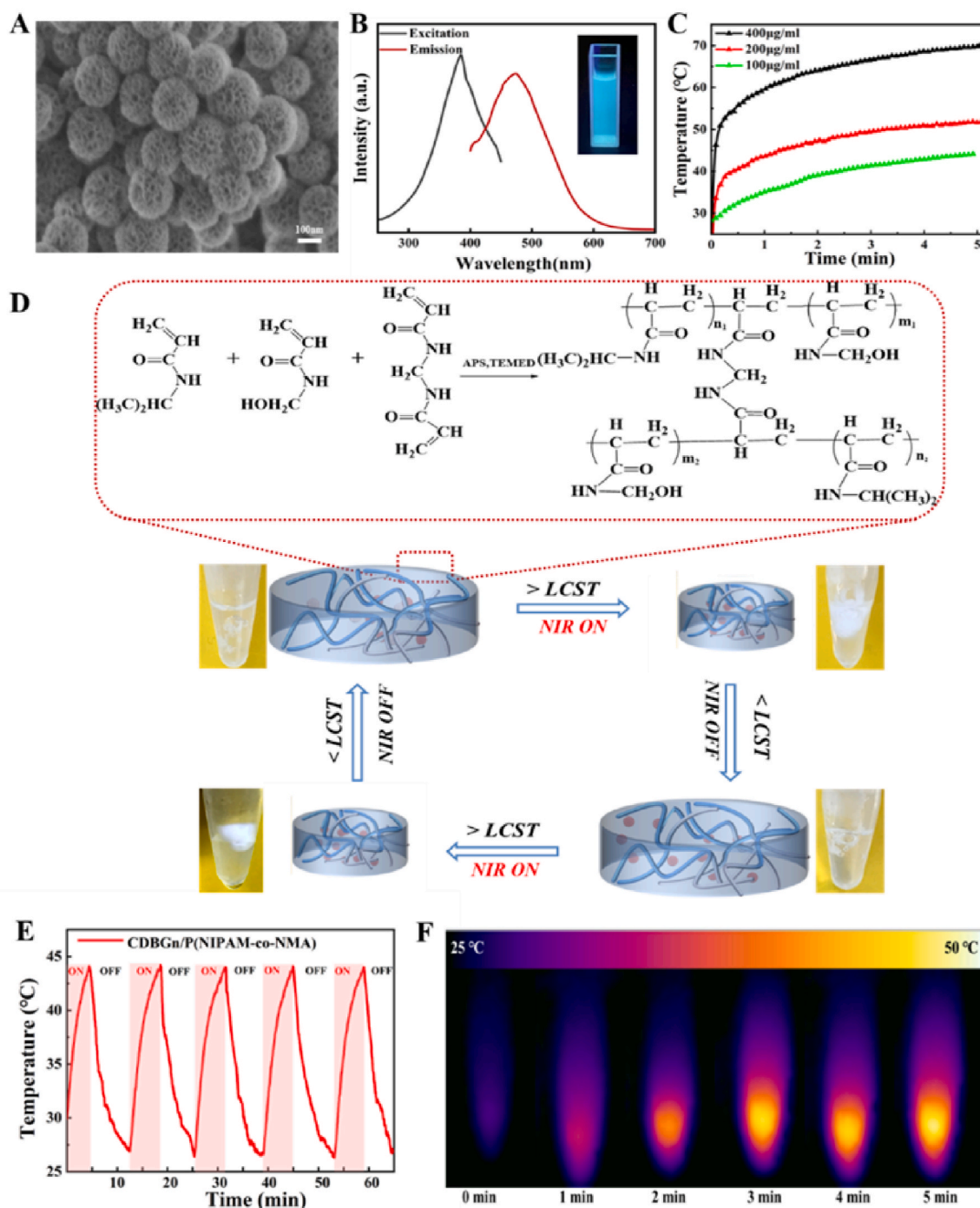


Fig. 2. Schematic illustration for the formation of CDBGn/P(NIPAM-co-NMA) hydrogel and photothermal behavior of CDBGn and the hydrogel. (A) SEM image of CDBGn. (B) Excitation and emission spectra of CDBGn in aqueous solution (inset: photograph of CDBGn aqueous suspension under 365 nm UV-light irradiation). (C) Temperature changes of CDBGn with different concentrations under NIR irradiation with a power of 1 W/cm². (D) Schematic illustration of the copolymer cross-linking reaction and NIR-driven variation of polymer hydrogel temperature and corresponding phase transition of polymer hydrogel. (E) Photothermal stability and (F) thermo-graphic images of CDBGn/P(NIPAM-co-NMA) hydrogel upon exposure to 808 nm NIR laser (1 W/cm²).

the desirable photothermal stability and recyclability of the hydrogel. Accordingly, the hydrogel underwent a reversible phase transition between swelling and shrink state during repeated “on/off” exposures to NIR irradiation (Fig. S6). Such NIR-responsive property of the hydrogel with suitable LCST confers its functionality as the “gating” to control the opening and closing of macro- and mesopores of MBG for the spatio-temporal control of PTHrP-2 release.

2.2. Characterization of MBG and CBP/MBGS

To achieve the efficient loading and delivery of PTHrP-2, the MBG scaffolds were constructed as PTHrP-2 carriers by a simple powder processing technique [44]. Figs. S7 and 3A-E show the overall appearance and hierarchically macro- and mesoporous structures of the resultant MBGS, respectively. It is observed that MBGS possesses an interconnected macroporous structure with pore sizes around 100–400

μm (Fig. 3A and B) and uniform mesoporous pores with an average diameter of 4.2 nm (Fig. 3C and D). The small-angle XRD pattern of MBGS (Fig. 3E) further demonstrates the existence of a highly ordered 2D-hexagonal mesoporous structure, which endows it with a large surface area of $658 \text{ m}^2/\text{g}$ and a high loading capacity for PTHrP-2, while its interconnected macroporous structure provides sufficient space for vascularization and new bone tissue formation as osteoblasts prefer to adhere to larger pores to mineralize bone and form new bone tissue with a graded porous structure [45,46]. Afterwards, the thermosensitive CDBGn/P(NIPAm-co-NMA) composite hydrogel was uniformly coated onto the macroporous walls of MBGS with a thickness of 10–20 μm , as revealed by the SEM image in Fig. 3F of the as-obtained CDBGn/P(NIPAm-co-NMA)-coated MBGS (denoted as CBP/MBGS). The freeze-dried CDBGn/P(NIPAm-co-NMA) hydrogels displayed a honeycomb-like structure with dense cell walls. The micropores within the coating layers were created by ice crystals within the network of swollen hydrogels after immersing the sample in liquid nitrogen. Moreover, the elemental mapping images (Fig. S8) of CBP/MBGS confirmed the presence of the layer on the scaffolds. After the hydrogel modification, the compressive strength of the MBGS increased from 0.8 to 1.2 MPa (Fig. 3G and H), indicating that the hydrogel coating-enabled adhesiveness could alleviate the crack propagation of the MBG matrix under mechanical stress. It is worth noting that the CDBGn/P(NIPAm-co-NMA) hydrogel layer can also appropriately slow down the degradation rate of the MBG scaffold. As demonstrated in Fig. 3I, compared with MBGS, CBP/MBGS shows a smaller and slower weight loss in PBS during the 28-day incubation period. Such gentler degradation of CBP/MBGS could eliminate the negative effects of rapid degradation of

MBG on cell attachment and growth for new bone formation, and make it match better with the rate of osteogenesis [47–49], thus facilitating the sustained release of the subsequently loaded PTHrP-2 and bone regeneration.

2.3. NIR-controlled PTHrP-2 release behaviors of CBP/MBGS/PTHrP-2

To investigate the NIR-controlled release capability of CBP/MBGS, the PTHrP-2 was immobilized into the mesopores of MBGS that were capped with the NIR-responsive CDBGn/P(NIPAm-co-NMA) hydrogel as a “gating”, as such CBP/MBGS/PTHrP-2 was fabricated. Prior to testing its PTHrP-2 release characteristics, the photothermal performance of CBP/MBGS was firstly evaluated. As shown in Fig. 4A and B, upon laser irradiation (808 nm, $1 \text{ W}/\text{cm}^2$), the temperature of CBP/MBGS increased rapidly and reached approximately $44 \text{ }^\circ\text{C}$ in 5 min even after five on/off cycles of NIR irradiation, which is identical to that of the CDBGn/P(NIPAm-co-NMA) hydrogel. This proves that the CBP/MBGS have photothermal conversion ability originating from their hydrogel coatings, which can further trigger the phase transition of the thermosensitive hydrogel gating to control the PTHrP-2 release from the pores. Subsequently, the NIR-controlled release behavior of PTHrP-2 from CBP/MBGS was tested. It is found that the release rate of PTHrP-2 in the CBP/MBGS/PTHrP-2 group significantly increased with laser irradiation and immediately slowed down with laser turned off, whereas that in the control group without irradiation or in the MBGS/PTHrP-2 group without hydrogel coatings, the release rate almost maintained steady during a period of 4 h (Fig. 4C and D). This indicates that the CBP/MBGS possesses good capability of NIR-induced dual-model (i. e. slow and

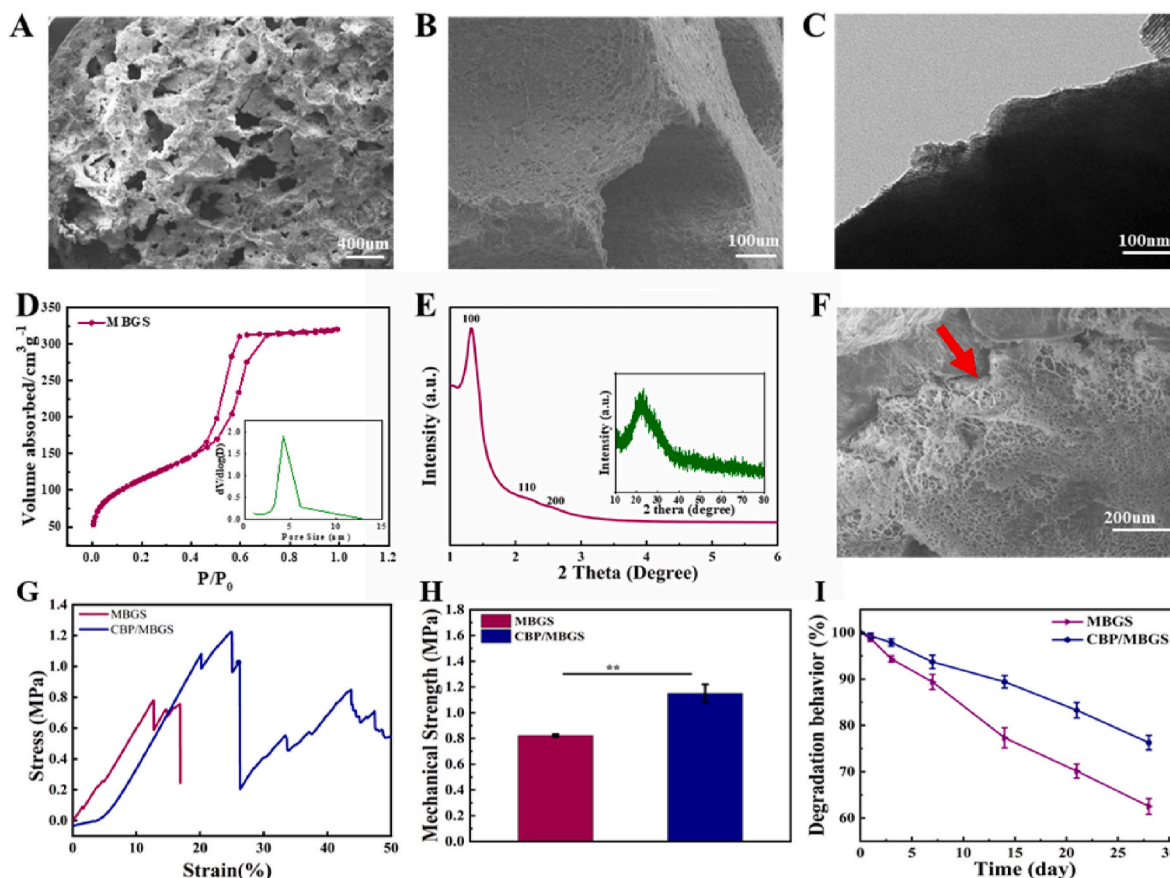


Fig. 3. Morphology and microstructural characterization of MBG and the composite MBG scaffolds. SEM images of the surface (A) and cross-section (B) of MBGS. (C) TEM image of the MBG powder. (D) N_2 adsorption-desorption isotherms and pore size distribution curve (inset) of MBGS. (E) SAXRD and WAXRD (inset) patterns of MBGS. (F) SEM image of the cross-section of CBP/MBGS, the red arrow indicates the CDBGn/P(NIPAm-co-NMA) coating layer. (G, H) Typical stress-strain curves and average mechanical strengths of MBGS and CBP/MBGS. (I) Degradation curves of MBGS and CBP/MBGS incubated in PBS at $37 \text{ }^\circ\text{C}$.

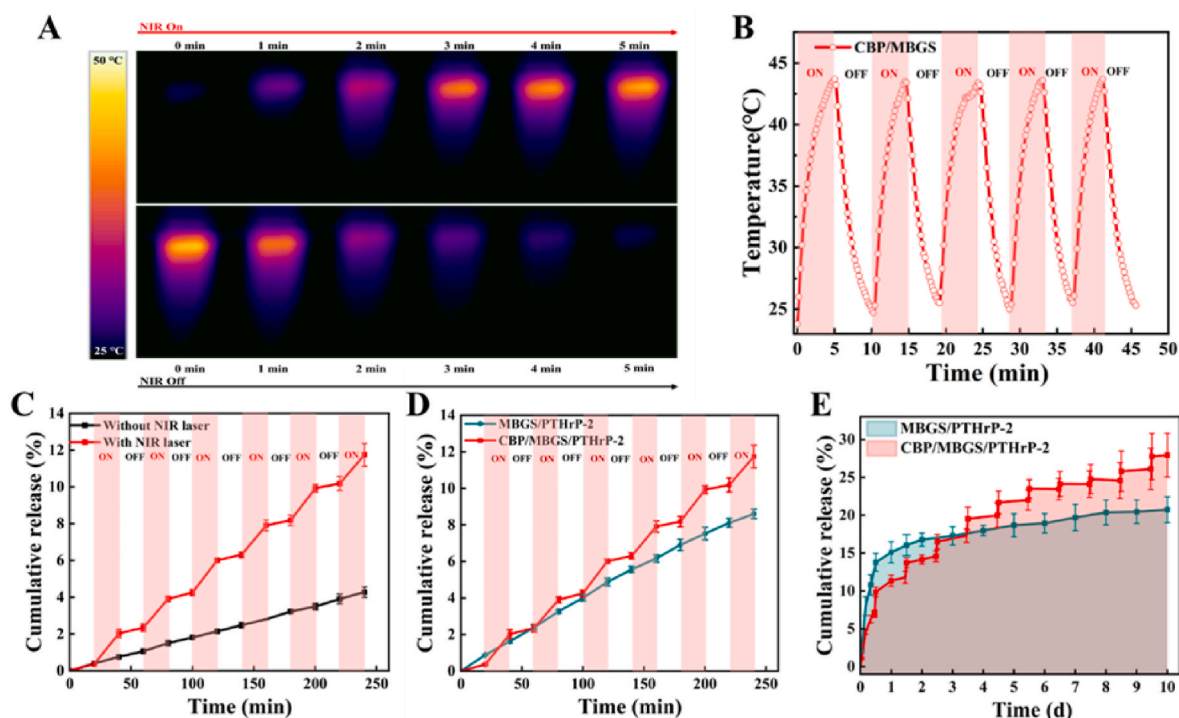


Fig. 4. Photothermal performance and controlled PTHrP-2 release from CBP/MBGS/PTHrP-2 *in vitro*. (A) Thermal images of CBP/MBGS upon exposure to an 808 nm NIR laser (5 min, 1 W/cm²). (B) Photothermal stability of CBP/MBGS under five on/off cycles of 808 nm laser irradiation (5 min, 1 W/cm²). (C) Release curve of PTHrP-2 from CBP/MBGS with periodic NIR irradiations (20 min) and without NIR irradiation, respectively. (D) Release curve of PTHrP-2 from CBP/MBGS and MBGS under periodic NIR irradiations (20 min), respectively. (E) *In vitro* long-term release of PTHrP-2 from CBP/MBGS and MBGS under successive on/off NIR laser irradiations during a 10-day period.

pulsatile) release, which can be ascribed to the thermosensitive phase transitions of the outer hydrogel gating. After 6 successive cycles of on/off irradiation, $11.7 \pm 0.6\%$ of PTHrP-2 was released from the CBP/MBG scaffolds, almost three times higher than that of the control group (Fig. 4C), and a lower PTHrP-2 release amount of $8.6 \pm 0.2\%$ was detected in the MBGS/PTHrP-2 group without CDBGn/P(NIPAM-co-NMA) hydrogel coatings (Fig. 4D). Furthermore, the *in vitro* long-term PTHrP-2 release profiles of CBP/MBGS/PTHrP-2 and MBGS/PTHrP-2 under repeated on/off laser irradiation over 10 days were studied. As shown in Fig. 4E, the CBP/MBGS/PTHrP-2 exhibit a pulsatile/slow dual-mode PTHrP-2 release behavior with a total release amount of 28% at the end of all cycles, while a burst release ($\sim 15\%$) of PTHrP-2 from the MBGS/PTHrP-2 was detected in 24 h and the release amount slightly increased to $\sim 20\%$ with a prolonged incubation time of 10 days (Fig. 4E). The above results collectively demonstrate that the CDBGn/P(NIPAM-co-NMA) hydrogel gating with both photothermal and thermoresponsive abilities allows the CBP/MBGS/PTHrP-2 to precisely control the release of PTHrP-2 through NIR at either a relatively slow or a pulsatile rate as desired. Such dual-mode release property of the CBP/MBG scaffold is expected to facilitate the on-demand release of PTHrP-2 at the bone defects to achieve an osteoclast/osteogenic balance and high-efficacy bone repair.

2.4. *In vitro* pro-osteogenic performances of CBP/MBGS/PTHrP-2

To evaluate the potential pro-osteogenesis ability of the CBP/MBGS/PTHrP-2 with NIR-driven dual-mode release property, the attachment, proliferation, differentiation, and gene expression of bone marrow stromal cells (BMSCs), which play important roles in the process of new bone formation, were measured after cultivated with different scaffolds. As observed in the CLSM images (Fig. 5A), after 24 h cultivation, the BMSCs were well adhered and spread on the surface of MBGS, MBGS/PTHrP-2 and CBP/MBGS/PTHrP-2, whose interconnected macropores

can provide space for cells to expand and grow. The BMSCs seeded on the MBGS and CBP/MBGS scaffolds maintained a sustained proliferation activity over the cultivation period, as assessed by the CCK-8 assay (Fig. 5B), verifying the excellent biocompatibility and cytocompatibility of the scaffolds. Subsequently, the proliferation of BMSCs treated with PTHrP-2-loaded scaffolds under 808 nm NIR irradiation conditions (1 W/cm², 10 min) was investigated (Fig. 5C). It is observed that a significant increase in the proliferation of BMSCs was detected in both CBP/MBGS/PTHrP-2 and MBGS/PTHrP-2 groups after 7 days of culture, and the CBP/MBGS/PTHrP-2 group exhibits an obviously stronger proliferative effect on BMSCs than the MBGS/PTHrP-2 or PTHrP-2-absence groups (Fig. 5B) on day 7, demonstrating that the NIR-triggered dual-mode PTHrP-2 release in the CBP/MBGS/PTHrP-2 effectively promotes the BMSCs proliferation. Furthermore, the osteogenic differentiation of BMSCs was analyzed by alkaline phosphatase (ALP) staining (Fig. 5D) and alizarin red staining (Fig. 5E), which confirms that all three scaffolds facilitate the BMSCs osteogenic differentiation, with the highest promoting efficacy in the CBP/MBGS/PTHrP-2 among them. In addition, the osteogenesis-related gene expressions were further investigated to prove the osteogenic ability. As shown in Fig. 5F–H, the relative expression levels of Col I, Runx2, BMP-2 were significantly up-regulated in the CBP/MBGS/PTHrP-2 group compared with those in other groups, suggesting the strongest osteogenic differentiation ability of CBP/MBGS/PTHrP-2, which is in good agreement with the ALP and alizarin red staining observations. These results confirm that the dual-mode PTHrP-2 delivery system (CBP/MBGS/PTHrP-2) possesses the outstanding capability to promote the proliferation and osteogenic differentiation of BMSCs *in vitro*.

2.5. *In vitro* proangiogenic capacity of CBP/MBGS/PTHrP-2

As the stimulation of angiogenesis is crucial for nutrient supply and bone formation during the skeletal development and fracture healing

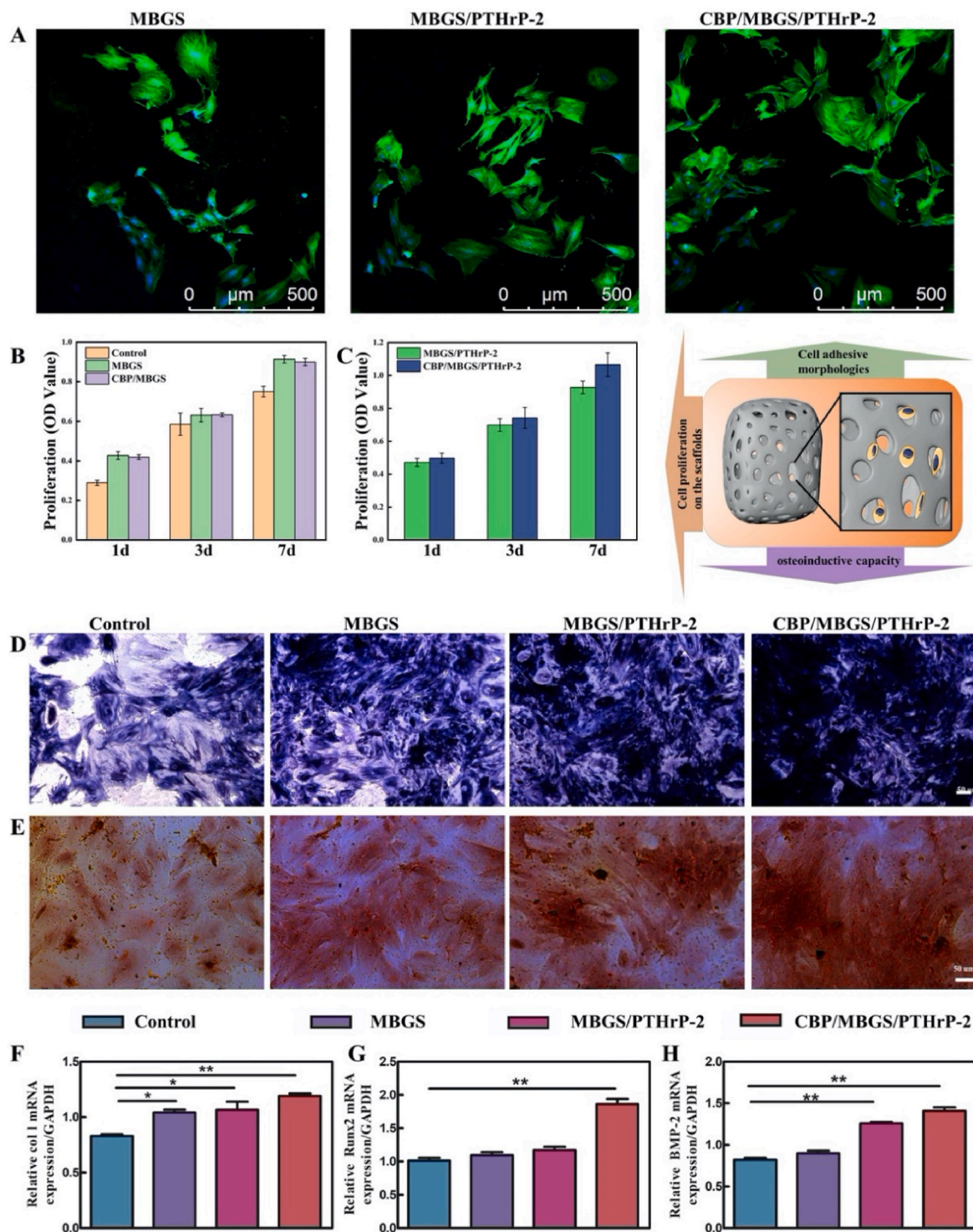


Fig. 5. *In vitro* proliferation and differentiation of BMSCs on different scaffolds. (A) Cell morphologies and attachment analysis of BMSCs on the surface of different scaffolds at 24 h. Green: cytoskeleton stained with FITC-Phalloidin, blue: cellular nuclei counterstained with DAPI. (B, C) The proliferation of BMSCs cultivated on the MBGS, CBP/MBGS and PTHrP-2-loaded scaffolds exposed to 808 nm laser irradiation (1 W/cm^2 , 10 min). (D) ALP staining of BMSCs cultured on different scaffolds at day 14. (E) Alizarin red staining of BMSCs mineral deposition on different scaffolds after 28 days. (F–H) Osteogenesis-related gene expressions of Col I (F), Runx2 (G), and BMP-2 (H) of BMSCs. *** $p < 0.001$, ** $p < 0.01$, * $p < 0.05$.

process [50,51], the proangiogenic capacity of CBP/MBGS/PTHrP-2 was thus estimated by monitoring the proliferation of human umbilical vein endothelial cells (HUVECs) [7,18,23]. As shown in Fig. 6A, compared with the control or PTHrP-2-absence group, PTHrP-2-loaded scaffolds significantly promote the proliferation of HUVECs to a greater extent at days 3 and 5, illustrating the proangiogenic effect of

PTHrP-2 in the scaffolds [23]. It is worth noting that the HUVECs proliferation rate of the CBP/MBGS/PTHrP-2 group is distinctly higher than that of the MBGS/PTHrP-2 group, which indicates that the dual-mode PTHrP-2 release of the CBP/MBGS/PTHrP-2 is more favorable for angiogenesis. Moreover, the migration of HUVECs treated with different scaffolds was evaluated by Transwell assays (Fig. 6B and D). It is found

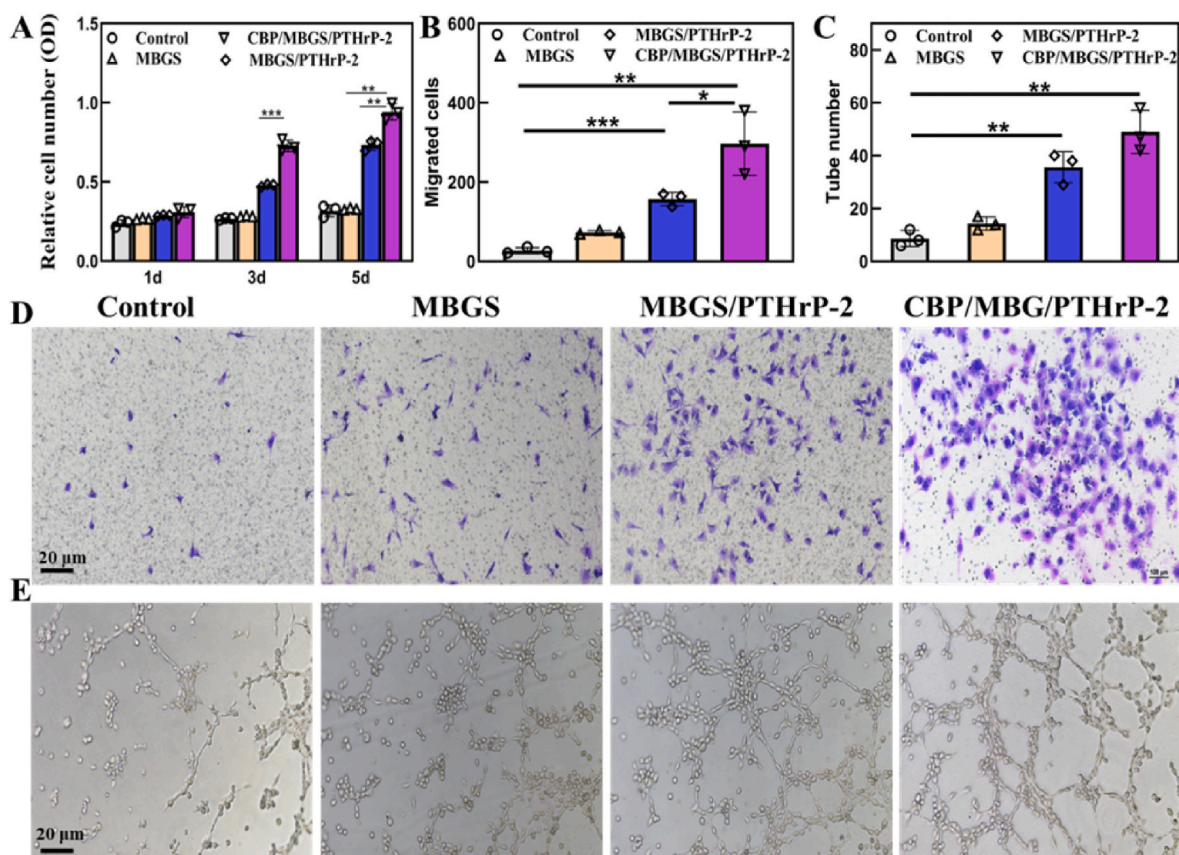


Fig. 6. HUVECs response to different scaffolds. (A–C) Quantitative analysis of the proliferation, migration, and tube numbers of HUVECs. (D, E) Representative photomicrographs of Transwell migration and tube formation of HUVECs. *** $P < 0.001$, ** $P < 0.01$, * $P < 0.05$.

that most HUVECs were transferred and recruited by CBP/MBGS/PTHrP-2 among all the groups, which can be attributed to its dual-mode PTHrP-2 release property. Tube forming assay was further conducted to observe vascularization, which reveals the formation of a meshwork of capillary-like structure in the CBP/MBGS/PTHrP-2 and MBGS/PTHrP-2 groups, with a higher tube number in the CBP/MBGS/PTHrP-2 group (Fig. 6C and E). In contrast, HUVECs in the control and MBGS groups maintained spherical and segregated with few short tubes and small cellular nests. Overall, these results demonstrate that slow and pulsatile PTHrP-2 release properties of the CBP/MBGS/PTHrP-2 efficiently promote angiogenesis *in vitro* via enhancing the proliferation, migration, and endothelial tube formation of HUVECs.

2.6. *In vivo* bone-forming and angiogenic effects of CBP/MBGS/PTHrP-2 on bone defect repair

To evaluate the bone regeneration capacity of the scaffolds *in vivo*, a rat model of critical-size femoral defects was established and implanted with MBGS, MBGS/PTHrP-2, and CBP/MBGS/PTHrP-2, respectively. The newly formed bone was observed by micro-CT with 3D reconstruction images (Fig. 7A and S9). It is shown that a significant amount of mineralized bone tissues was formed on the surface of local femur defects in the CBP/MBGS/PTHrP-2 group, however, much less newly formed bone in the MBGS group was found around the defect edges without any bridges formed across the bone defects. The anterior-posterior, cross-sectional, and lateral Micro-CT images also reveal the highest amount of newly formed bone in the CBP/MBGS/PTHrP-2 group compared to the other groups. Consistent with this finding, the CBP/MBGS/PTHrP-2 group exhibits superior femur trabecular bone micro-architecture with obviously higher bone mineral density (BMD; 0.2 g/

cc), bone volume/total volume (BV/TV; 59.6%), and trabecular thickness (Tb.Th: 0.35) and numbers (Tb.N: 2.32) than those in the other groups, demonstrating the notable bone regeneration ability of the NIR-activated dual-mode delivery system of CBP/MBGS/PTHrP-2. Similar results could be found in Van Gieson staining (Fig. 8A and B), where the CBP/MBGS/PTHrP-2 group exhibits highest bone regeneration performance among all the groups, while the MBGS is mostly resorbed with a low conversion rate and poor defects repair. Further, immunohistochemical staining for CD31/ α -SMA was employed to evaluate the newly-formed vessels, since the formation of mature blood vessels is surrounded by smooth muscle cells that can be identified by staining the α -SMA protein. As shown in Fig. 8C–E and Fig. S10, the maximum amount of neo-vascularization at the bone defects implanted with CBP/MBGS/PTHrP-2 was observed. However, the treatment with MBGS and MBGS/PTHrP-2 barely induces newly visible vascular formation around the implant. This phenomenon can be attributed to the NIR-controlled long-term sustained and on-demand pulsatile release of PTHrP-2 by the CBP/MBGS/PTHrP-2, which enables it to continually stimulate early vascularization and promote more osteoblasts to participate in the bone remodeling, thus resulting in a remarkably improved bone reparative effect [52]. In contrast, the burst PTHrP-2 release of MBGS/PTHrP-2 prevented it from supplying sustained and sufficient PTHrP-2 to trigger angiogenesis for bone regeneration. Such precisely controlled delivery of PTHrP-2 by the CBP/MBGS/PTHrP-2 is thus demonstrated to be a feasible strategy to effectively induce local angiogenesis and bone reconstruction *in vivo*.

3. Conclusion

In summary, we have fabricated a novel dual-mode PTHrP-2 delivery system (CBP/MBGS/PTHrP-2) for bone defect repair and regeneration

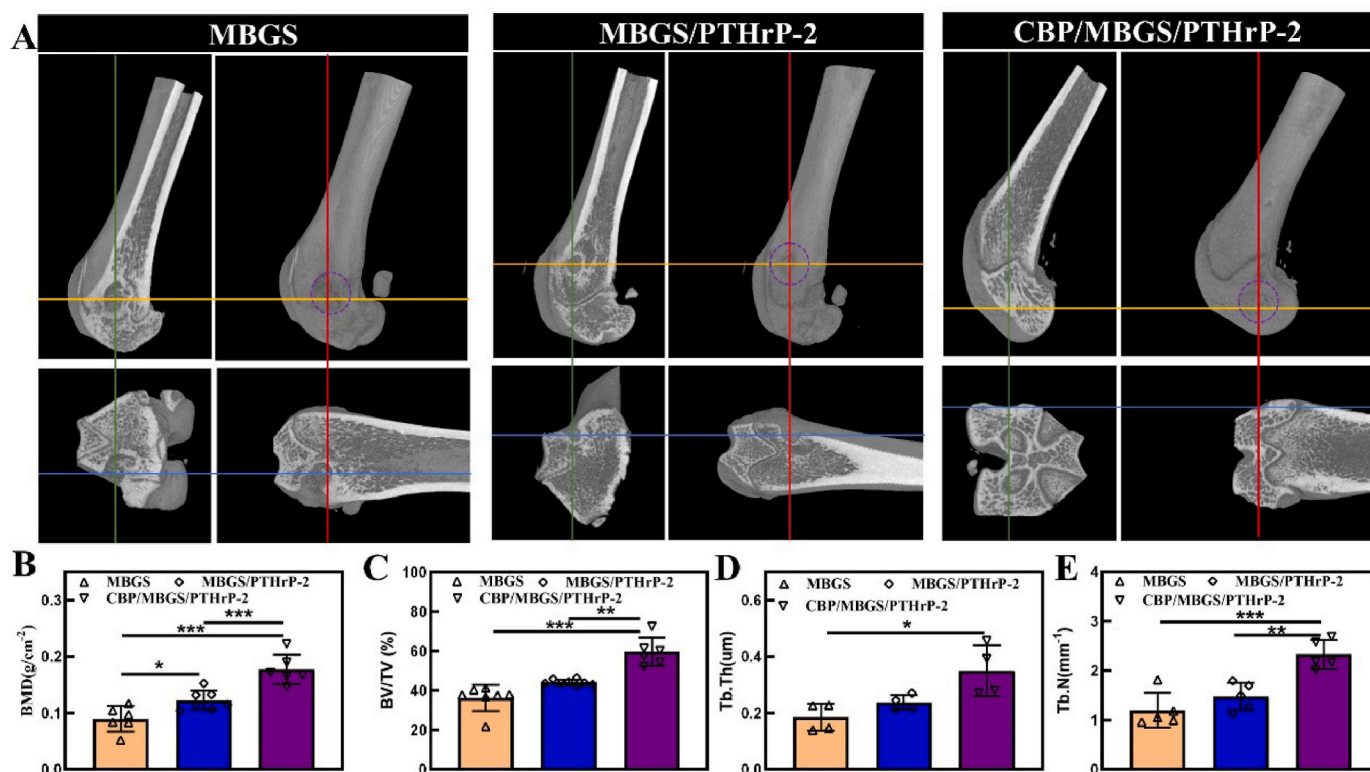


Fig. 7. Analysis of bone formation in the femurs defect model. (A) 3D micro-CT rendered reconstruction and anterior-posterior, cross-sectional, and lateral micro-CT images of the femur defect site. (B–E) Quantitative analysis of bone volume/total volume (BV/TV), bone mineral density (BMD), trabecular thickness (Tb.Th) and trabecular number (Tb.N). * $P < 0.05$, ** $P < 0.01$, *** $P < 0.001$.

based on a NIR-stimulated thermosensitive hydrogel-coated MBG bio-scaffold. In the designed system, the CDBGn/P(NIPAM-co-NMA) hydrogel shell with both photothermal and thermoresponsive ability serves as a NIR-driven gating to accurately control the release of PTHrP-2 from the mesopores of MBGS at either a relatively slow or a pulsatile rate as desired, constantly promoting the proliferation and osteogenic differentiation of BMSCs as well as the proliferation, migration, and endothelial tube formation of HUVECs via a well-maintained sufficient PTHrP-2 concentration at the bone defect sites. Meanwhile, the interconnected porous structure of MBGS provides adequate spaces for the recruitment, proliferation, and differentiation of osteoblast-related cells and bone tissue formation. As a result, such a precise dual-mode release system with a hierarchically porous structure and good mechanical strength exhibits both strong pro-osteogenic and pro-angiogenic effects on bone defects *in vitro* and *in vivo*, cooperatively improving the bone repair efficacy for critical-size femoral defects. This unique design of the precisely controlled dual-mode delivery system provides inspiration for engineering novel bone repair and regeneration materials to advance the development of regenerative medicine.

4. Experimental section

4.1. Materials

MEM culture medium, PBS, and fetal bovine serum were purchased from Gibco (Thermo Fisher Scientific Inc. MA, USA). N-isopropylacrylamide (NIPAm), and N-Methylol acrylamide (NMA, 48%) were obtained from Aladdin Biochemical Technology Co. Ltd (Shanghai, China). N,N,N',N'-Tetramethylethylenediamine (TEMED), ammonium persulfate (APS), and N,N-Methylenebisacrylamide Bis-acrylamide (MAB) were obtained from Shanghai Macklin Biochemical Co. Ltd. P123 (Mw = 5800, EO₂₀PO₇₀EO₂₀), Ca(NO₃)₂·4H₂O, tetraethyl orthosilicate (TEOS) and triethyl phosphate (TEP) were purchased from Lingfeng

Chemical Reagent Co. Ltd (China). The amphiphilic block copolymer PS₁₃₁-b-PAA₁₆ was synthesized via the sequential atomic transfer radical polymerization (ATRP) method reported by Kang et al. [53]. Polyvinylpyrrolidone (PVP, K30), polyethyleneglycol (PEG, Mw = 6000), tetrahydrofuran (THF, AR), and ethanol (AR) were obtained from Shanghai Titan Chemical Reagent Co., Ltd. Cetyltrimethyl ammonium bromide (CTAB, ≥99%) and 3-Aminopropyltriethoxysilane (APTES, 97%) were purchased from Aladdin. PTHrP-2rP-2 was provided by the Sixth People's Hospital (Shanghai, China).

4.2. Preparation of CDBGn

For the preparation of CDBGn, PS-*b*-PAA (25 mg) was dissolved in THF (5 mL) with vigorous stirring at room temperature. Then the clear oil solution was poured into CTAB aqueous solution containing CTAB (40 mg), distilled water (20 mL) and 28% ammonia (250 μL), and the inorganic sources (Ca(NO₃)₂·4H₂O, TEOS) were added step by step at an interval of 10 min. After stirring for 24 h at room temperature, the product was collected by centrifugation (10000 rpm) and was washed with ethanol and water and dried at room temperature. The template was removed by calcination at 550 °C for 4 h. After obtaining BGN nanoparticles, APTES was used to graft amino groups on the surface of BGN. Briefly, BGN was added into 50 mL of dry toluene with certain amount of APTES (APTES: SiO₂ = 0.3:1, molar ratio) and the mixture was heated under reflux for 12 h at 80 °C, followed by centrifugation and rinsed with Milli-Q water and toluene several times, and dried under vacuum at 80 °C, to obtain the amino-modified BGN. Finally, the CDS-doped BGN (CDBGn) was obtained by heating at 400 °C for 2 h in air.

4.3. Synthesis of P(NIPAm-co-NMA) and CDBGn/P(NIPAm-co-NMA) (CBP)

Firstly, dried nitrogen was bubbled through the solution for 10min

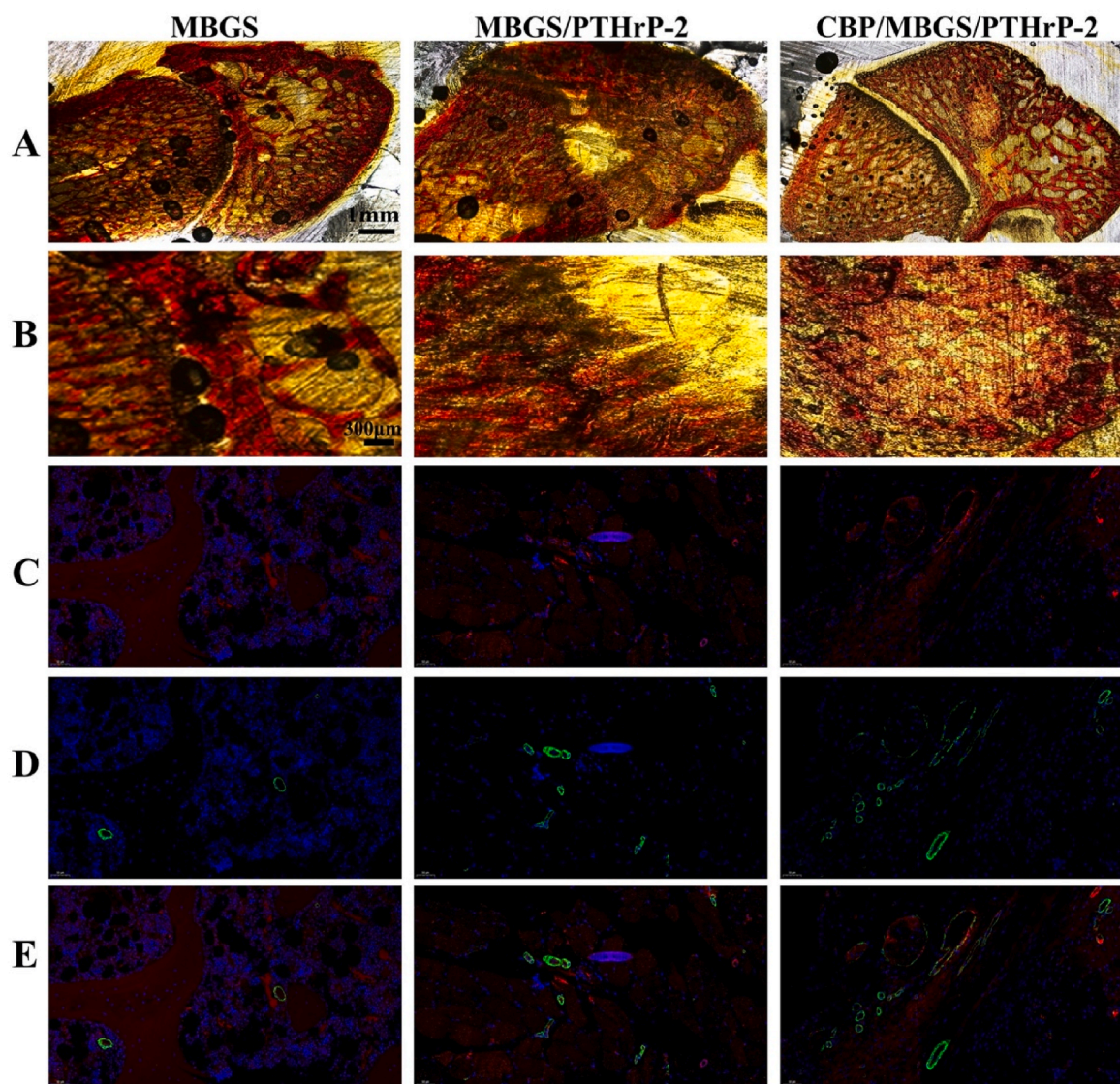


Fig. 8. Histological evaluation of new bone regeneration and vessel formation at week 8 post-implantation for different implants. (A, B) Van Gieson's staining of the newly formed bone (red color). (C–E) Newly formed blood vessels observed by immunofluorescent staining for CD31 and α -SMA. Vascular endothelial cells (CD31), smooth muscle cells (α -SMA), and cell nuclei are stained in red, green, and blue, respectively. Red and green co-staining represents mature blood vessels.

before polymerization. The pregel solutions consisting of the mixture of NIPAm and NMA at molar ratios of 10:1 and 8:1 and MBA (1% w/w) were dissolved in deionized water. Afterwards, polymerization was initiated and accelerated by APS and TEMED (2% v/v). The hydrogel was then placed at 10 °C for 24 h and soaked in deionized water for 2 days to remove surfactant and other unpolymerized small molecules. To synthesize CDBGn/P(NIPAm-co-NMA), CDBGn was dispersed in water and ultrasonication was applied to the mixture for 30 min, followed by the process mentioned above.

4.4. Preparation of MBGS, MBGS/PTHrP-2 and CBP/MBGS/PTHrP-2

MBG80S15C (S and C are SiO₂ and CaO, respectively) was demonstrated to process the best bioactivity and was prepared through evaporation-induced self-assembly (EISA) [44,54,55]. Briefly, 4.0 g of P123, 6.7 g of TEOS, 1.4 g of Ca(NO₃)₂·4H₂O, 0.73 g of TEP and 1.0 g of HCl (0.5 M) were dissolved in 60 g of ethanol and stirred at room temperature for 24 h, and the resulting sol was cast into a Petri dish to undergo an EISA process [55]. The dried gel was calcined at 700 °C for 5 h and the obtained MBG was then ground and sieved into powders with a

particle size range of 40–50 μ m. The MBG scaffolds were prepared according to our previous method [44]. Typically, PVP and PEG particles (about 300–400 μ m) were used as porogen. MBG powders, PVP and PEG particles (MBG: PVP: PEG = 1:0.2:1) were mixed well for 4 h and then poured into a cylinder mold with a specific diameter. The mold containing the mixture was pressed at 5 MPa to obtain a cylindrical green body and calcined at 600 °C (ramp of 1 °C/min) for 5 h to obtain the MBGS. MBGS with different sizes and shapes were prepared by using various molds. PTHrP-2 was then immobilized in the MBGS before CDBGn/P(NIPAm-co-NMA)(CBP) coating, and all scaffolds were sterilized by gamma irradiation. The traditional drug immobilization strategy is to immerse the scaffold in the drug solutions overnight, resulting in an uncontrollable amount of immobilization. Hence, a dipping and lyophilizing method was used to immobilize PTHrP-2 into the mesopores of MBGS as reported in previous studies [47,48]. 0.1 mg/mL of PTHrP-2 was added dropwise to each scaffold under a sterile condition, followed by keeping the solution for 6 h to achieve full adsorption of PTHrP-2 into the mesopores of MBGS at 4 °C and vacuum-freeze dried overnight. Finally, MBGS and MBGS/PTHrP-2 were added to the pregel solution and the CBP hydrogel was uniformly coated onto the surface of

MBGS and MBGS/PTHrP-2.

4.5. Characterizations

The microporous walls, inner mesoporous microstructure and phase composition of the scaffolds were confirmed by scanning electron microscopy (SEM, Hitachi S-4800), X-ray diffraction (XRD), transmission electron microscopy (TEM, JEM 2100F). The specific surface areas, pore volumes and pore size distributions were determined by Brunauer-Emmett-Teller (BET) and Barrett-Joyner-Halenda (BJH) analysis (Micromeritics Tristar 3020). The fluorescent properties and excitation/emission curves of CDBGn in aqueous solution were measured on an Edinburgh FS-5 fluorescence spectrophotometer. And the digital photo of CDBGn suspension under irradiation with a UV lamp ($\lambda = 365$ nm) was taken with a cellphone. The XPS investigation was carried out on a Thermo Scientific K-Alpha instrument to analyze the elements constituting the sample surface of CDBGn. Raman spectra were obtained using Laser Micro-Raman Spectromete. To measure the phase transition and stability of the hydrogel, samples were placed directly in a pre-heated thermostat water bath at 41 °C and then taken out to be cooled naturally. The compressive strength was tested using a computer-controlled universal testing machine (HY-0230) at a cross-head speed of 0.5 mm/min. The degradation behaviors of the scaffolds were characterized by monitoring the weight loss. Specifically, the initially prepared cylindrical scaffolds were dried and weighed (W0), and then the dried samples were immersed in PBS and incubated under a constant temperature (37 °C, 100 rpm) according to international standards (ISO 10993-14:2001, IDT), during which the scaffolds were dried and weighed (Wt) at corresponding time points. The LCST of the hydrogel was measured by Differential Scanning Calorimetry (DSC), where the hydrogel was wetted with water for 24 h and put into DSC cells, and then the DSC thermograms were obtained at a heating rate of 5 °C/min from 0 to 80 °C using the DSC2910 system.

4.6. Photothermal properties and *in vitro* PTHrP-2 release upon NIR stimulation

The photothermal properties of CDBGn solutions (400 µg/mL, 200 µg/mL, 100 µg/mL) and CDBGn/P(NIPAm-co-NMA) hydrogels were studied using an 808 nm NIR laser (1 W/cm², Hps3200). To verify the photothermal stability of CDBGn/P(NIPAm-co-NMA) hydrogels and CBP/MBG scaffolds, the ON/OFF laser irradiation procedure was repeated for five cycles. The real-time temperature changes were monitored by an IR camera (FOTRIC 227). To evaluate volume changes modulated by photothermal stability, swollen hydrogels were exposed to an NIR laser, and then the laser was shut down to cool down the temperature of hydrogels to room temperature.

For the continuous release profile of PTHrP-2, MBGS/PTHrP-2 scaffolds were placed in vials containing 5 mL phosphate-buffered saline (PBS, pH = 7.4) and then shaken at 37 °C under a constant vibration of 80 rpm. At each time point, the release medium was collected and replaced with the same volume of fresh PBS. To study the NIR-activated PTHrP-2 release, the CBP/MBG/PTHrP-2 was irradiated for 20 min with an 808 nm laser (1 W/cm²) and left for another 20 min without laser exposure for six cycles. Furthermore, a 10-day long-term dual-mode PTHrP-2 release test was performed. Scaffolds were irradiated for 20 min every 24 h until 10 cycles were completed, and all the collected suspensions were evaluated by UV-Vis spectrum.

4.7. *In vitro* cell studies

4.7.1. Bone marrow stromal cells (BMSCs) culture and cell proliferation on scaffolds

In vitro studies on osteogenesis were performed using BMSCs. First, 100 g SD rats were sacrificed by dislocation and soaked in 75% ethanol for 5 min, and then the BMSCs isolation was achieved by gradient

centrifugation for 5 min. The cells were resuspended in α -MEM supplemented with 10% FBS, 1% penicillin/streptomycin and cultured in a humidified incubator containing 5% CO₂ at 37 °C. The adhesion and spreading of BMSCs culture on different scaffolds were examined after 24 h. The effect of each scaffold on the proliferation of BMSCs was tested by CCK-8 which provides a convenient way of performing a cell viability assay. The CBP/MBGS/PTHrP-2 group was co-cultured with BMSCs, and the cells were irradiated with 808 nm NIR for 10 min. This irradiation procedure was repeated once a day. After incubation for 3 and 7 days, the CCK-8 assay was performed according to the manufacturer's instructions. In this study, a collection of human umbilical vein endothelial cells (HUVECs) was obtained from the Cell Bank of the Institute of Biochemistry and Cell Biology, SIBS, CAS (Shanghai, China) and was used to evaluate the induced angiogenesis *in vitro*.

4.7.2. ALP activity and ASR staining

Alkaline phosphate (ALP) activity, which is an early marker of BMSCs differentiation, was measured to evaluate the osteogenic differentiation of BMSCs cultured with different scaffolds. BMSCs were seeded on each scaffold and at different time points, then the scaffolds were washed with phosphate buffered saline (PBS) three times and lysed in 0.2% Triton™ X-100 (Sigma Aldrich, Australia) to each well. Centrifuge samples at 4 °C at top speed for 15 min to remove any insoluble material. Add 50 µL of 5 mM pNPP solution to all samples and background control wells, incubated for 30 min at 37 °C according to the manufacture protocol (Alkaline Phosphatase Assay Kit, Beyotime Biotechnology, China) and ALP staining was performed according to the manufacturer's instructions of BCIP/NBT Alkaline Phosphatase Color Development Kit (Beyotime Biotechnology, China). For the ASR staining, the BMSCs were cultured with scaffolds and osteogenic differentiation basal medium for 28 days. At the end of the incubation time, the culture medium was removed and the BMSCs were fixed with 4% formaldehyde for 15 min at room temperature. Removed the fixative and washed the cells 3 times with PBS, fixed BMSCs were stained with ARS solution (pH 4.2) for 10 min at room temperature. And the ALP and alizarin red staining of the BMSCs was observed by an inverted light microscope (TE2000U, Nikon Corp., Japan).

4.7.3. Real-time quantitative PCR (qRT-PCR) analysis for osteogenic expressions of BMSCs on different scaffolds

Osteogenic gene expressions were measured by the qRT-PCR system and osteogenic differentiation markers: Col I, runt-related transcription factor 2 (Runx2), and BMP-2 were evaluated. The sequences of primers are listed in Table S1. Col I, Runx2, and BMP-2 gene expression in BMSCs separately were measured on day 7 by qRT-PCR system. Total RNA was isolated from cell pellets with TRIzol Reagent (Invitrogen). Complementary DNA was synthesized from total RNA using a RevertAid First Strand 88cDNA Synthesis Kit (Thermo Scientific) following the manufacturer's protocol. The qRT-PCR was performed using the ABI Prism 7300 Sequence Detection System (Applied Biosystems, Australia) using SYBR® Green detection reagent. The mean cycle threshold (Ct) value of each target gene was normalized against the Ct value of GAPDH and the relative expression was calculated using the following formula: $2^{-(\text{normalized average Cts})} \times 10^4$.

4.7.4. Cell proliferation, migration and tube formation assays of HUVECs

The proliferation of HUVECs was seeded on the scaffolds and incubated for 12 h in a manner similar to that used for BMSCs. The migration of HUVECs was assessed via Transwell assays. 2×10^4 HUVECs were used in the upper chamber in a Transwell apparatus (Coring, USA) and the scaffolds were placed into the lower chamber. The cells passed through the polycarbonate membrane and cling to the bottom side, after removal of non-migratory cells, the migratory HUVECs were stained with 0.5% crystal violet. To analyze the tube formation, the cold ECM gel (50 µL, BD Bioscience, USA) with a precooled tip was added to a 96-well plate. Following that, the HUVEC suspension (1.5×10^5 , 100 µL)

pretreated with different scaffolds was added to the ECM gel and incubated for 15 min. The results were quantified 8 h later. The tube structures formed in the gel were photographed using a light microscope.

4.8. Surgical procedures and Micro-CT imaging analysis

The Animal Ethical Committee at the Sixth People's Hospital (Shanghai, China) affiliated with Shanghai Jiao Tong University reviewed and approved all animal experimental procedures (License number: SCXK (Hu) 2018-0004). Male Sprague-Dawley (SD) rats (body weight: 280–300 g) were used for the experiments. After anesthetization through intraperitoneal injection of pentobarbital sodium (35 mg/kg), cylindrical defects ($d = 2.5$ mm, $h = 2$ mm) were created in the distal end of the rats' femurs (both left and right legs) before implanting the scaffolds. After 8 weeks, radiographic and histological analyses were conducted on each group ($n = 6$). All of the SD rats were sacrificed and all femurs were collected at 8 weeks for micro-CT scanning (SkyScan 1176). The samples were scanned and reconstructed using 3D creator software. And the parameters such as bone mineral density (BMD), bone volume (BV/TV), trabecular number (Tb.N), and trabecular separation (Tb.Sp) were calculated.

4.9. Histological and immunohistochemical staining

To observe new bone formation microscopically, the bone sections were dehydrated with graded ethanol solution and embedded in polymethylmethacrylate. Then the samples were stained with van Gieson's stain and observed by an optical microscope to evaluate the bone regeneration. Immunofluorescence staining of the thin sections was performed to study the angiogenesis of the bone defect areas. Immunofluorescence staining for CD31 and alpha-smooth actin (α -SMA), a marker of vascular smooth muscle cells (Abcam, Cambridge, UK), were performed to observe the regenerated capillaries.

4.10. Statistical analysis

All data are shown as the means and standard deviations and all data were collected from at least three independent experiments. Statistical analysis was performed using software Origin 2019 and Prism 8. The mean values were analyzed by one-way ANOVA with post hoc tests. $*p < 0.05$ were considered statistically significant.

Ethics approval and consent to participate

All animal experiments were carried out according to the guidelines approved by the Animal Research Committee of Sixth People's Hospital, Shanghai Jiao Tong University School of Medicine.

CRediT authorship contribution statement

Shi Liu: Conceptualization, Investigation, Methodology, Formal analysis, Data curation, Validation, Writing – original draft. **Zhengzhe Han:** Investigation, Methodology, Formal analysis, Resources. **Ji-Na Hao:** Investigation, Visualization, Supervision, Writing – review & editing. **Dapeng Zhang:** Writing – review & editing. **Xianglong Li:** Supervision. **Yuanyuan Cao:** Supervision. **Jinghuan Huang:** Methodology, Supervision, Resources. **Yongsheng Li:** Conceptualization, Supervision, Project administration, Writing – review & editing, Funding acquisition.

Declaration of competing interest

The authors declare that they have no known competing financial interests or personal relationships that could have appeared to influence the work reported in this paper.

Acknowledgements

This work was financially supported by the National Key Research and Development Program of China (Grant No. 2022YFC2403203), the National Natural Science Foundation of China (Nos. 51972112, 82202695, and 52172279), Basic Research Program of Shanghai (21JC1406003 and 19JC1411700), Leading Talents in Shanghai in 2018, Shanghai Rising Star Program (21QA1402200), the Natural Science Foundation of Shanghai (21ZR1416600), and the 111 project (B14018).

Appendix B. Supplementary data

Supplementary data to this article can be found online at <https://doi.org/10.1016/j.bioactmat.2023.02.008>.

References

- [1] G.L. Koons, M. Diba, A.G. Mikos, Materials design for bone-tissue engineering, *Nat. Rev. Mater.* 5 (2020) 584–603.
- [2] Anna M. McDermott, Samuel Herberg, Devon E. Mason, Joseph M. Collins, Hope B. Pearson, James H. Dawahare, Rui Tang, Amit N. Patwa, Mark W. Grinstaff, Daniel J. Kelly, Eben Alsberg, J.D. Boerckel, Recapitulating bone development through engineered mesenchymal condensations and mechanical cues for tissue regeneration, *Sci. Transl. Med.* 11 (2019), eaav7756.
- [3] R. Li, C. Zhou, J. Chen, H. Luo, R. Li, D. Chen, X. Zou, W. Wang, Synergistic osteogenic and angiogenic effects of KP and QK peptides incorporated with an injectable and self-healing hydrogel for efficient bone regeneration, *Bioact. Mater.* 18 (2022) 267–283.
- [4] W.E.G. Müller, S. Wang, M. Ackermann, T. Gerich, M. Neufurth, M. Wiens, H. C. Schröder, X. Wang, Biologization of allogeneic bone grafts with polyphosphate: a route to a biomimetic periosteum, *Adv. Funct. Mater.* 29 (2019), 1905220.
- [5] S. Herberg, A.M. McDermott, P.N. Dang, D.S. Alt, R. Tang, J.H. Dawahare, D. Varghai, J.Y. Shin, A. McMillan, A.D. Dikina, F. He, Y.B. Lee, Y. Cheng, K. Umemori, P.C. Wong, H. Park, J.D. Boerckel, E. Alsberg, Combinatorial morphogenetic and mechanical cues to mimic bone development for defect repair, *Sci. Adv.* 5 (2019), eaax2476.
- [6] S. Bhumiratana, J.C. Bernhardt, D.M. Alfi, K. Yeager, R.E. Eton, J. Bova, F. Shah, J. M. Gimble, M.J. Lopez, S.B. Eising, G. Vunjak-Novakovic, Tissue-engineered autologous grafts for facial bone reconstruction, *Sci. Transl. Med.* 8 (2016) 343ra383.
- [7] L. Jiang, W. Zhang, L. Wei, Q. Zhou, G. Yang, N. Qian, Y. Tang, Y. Gao, X. Jiang, Early effects of parathyroid hormone on vascularized bone regeneration and implant osseointegration in aged rats, *Biomaterials* 179 (2018) 15–28.
- [8] X. Liu, Y. Miao, H. Liang, J. Diao, L. Hao, Z. Shi, N. Zhao, Y. Wang, 3D-printed bioactive ceramic scaffolds with biomimetic micro/nano-HAp surfaces mediated cell fate and promoted bone augmentation of the bone-implant interface in vivo, *Bioact. Mater.* 12 (2022) 120–132.
- [9] S. Jana, S.K. Levegood, M. Zhang, Anisotropic materials for skeletal-muscle-tissue engineering, *Adv. Mater.* 28 (2016) 10588–10612.
- [10] C. Zhu, S. Pongkitwitoon, J. Qiu, S. Thomopoulos, Y. Xia, Design and fabrication of a hierarchically structured scaffold for tendon-to-bone repair, *Adv. Mater.* 30 (2018), e1707306.
- [11] G. Brabant, K. Prank, C. Schoff, Pulsatile patterns in hormone secretion, *Trends Endocrinol. Metabol.* 3 (1992) 183–190.
- [12] N. Goldenberg, J.F. Horowitz, A. Gorgey, A. Sakharova, A.L. Barkan, Role of pulsatile growth hormone (GH) secretion in the regulation of lipolysis in fasting humans, *Clin. Diabet. Endocrinol.* 8 (2022).
- [13] R. Tsutsumi, N.J.G. Webster, GnRH pulsatility, the pituitary response and reproductive dysfunction, *Endocr. J.* 56 (2009) 729–737.
- [14] M. Homme, F. Schaefer, O. Mehls, C.P. Schmitt, Differential regulation of RGS-2 by constant and oscillating PTH concentrations, *Calcif. Tissue Int.* 84 (2009) 305–312.
- [15] V. Shen, D.W. Dempster, R. Birchman, R. Xu, R. Lindsay, Loss of cancellous bone mass and connectivity in ovariectomized rats can be restored by combined treatment with parathyroid hormone and estradiol, *J. Clin. Invest.* 91 (1993) 2479–2487.
- [16] S. Starling, Insights into parathyroid hormone secretion, *Nat. Rev. Endocrinol.* 16 (2020) 256–257.
- [17] M.N. Wein, Y. Liang, O. Goransson, T.B. Sundberg, J. Wang, E.A. Williams, M. J. O'Meara, N. Govea, B. Beqo, S. Nishimori, K. Nagano, D.J. Brooks, J.S. Martins, B. Corbin, A. Anselmo, R. Sadreyev, J.Y. Wu, K. Sakamoto, M. Foretz, R.J. Xavier, R. Baron, M.L. Bouxsein, T.J. Gardella, P. Divieti-Pajevic, N.S. Gray, H. M. Kronenberg, SIKs control osteocyte responses to parathyroid hormone, *Nat. Commun.* 7 (2016), 13176.
- [18] J.N. Smith, J.M. Weber, L.M. Calvi, PTH stimulates osteoblastic VEGF-A production and remodels bone marrow micro-endothelial structures, *Blood* 118 (2011) 722, 722.
- [19] H.L. Chan, L.K. McCauley, Parathyroid hormone applications in the craniofacial skeleton, *J. Dent. Res.* 92 (2013) 18–25.

- [20] R.W. Cheloha, S.H. Gellman, J.P. Vilaradaga, T.J. Gardella, PTH receptor-1 signalling-mechanistic insights and therapeutic prospects, *Nat. Rev. Endocrinol.* 11 (2015) 712–724.
- [21] M. Dang, A.J. Koh, X. Jin, L.K. McCauley, P.X. Ma, Local pulsatile PTH delivery regenerates bone defects via enhanced bone remodeling in a cell-free scaffold, *Biomaterials* 114 (2017) 1–9.
- [22] X. Liu, G.J. Pettway, L.K. McCauley, P.X. Ma, Pulsatile release of parathyroid hormone from an implantable delivery system, *Biomaterials* 28 (2007) 4124–4131.
- [23] J. Huang, D. Lin, Z. Wei, Q. Li, J. Zheng, Q. Zheng, L. Cai, X. Li, Y. Yuan, J. Li, Parathyroid hormone derivative with reduced osteoclastic activity promoted bone regeneration via synergistic bone remodeling and angiogenesis, *Small* 16 (2020), e1905876.
- [24] J. Li, Q. Zheng, X. Guo, Z. Zou, Y. Liu, S. Lan, L. Chen, Y. Deng, Bone induction by surface-double-modified true bone ceramics in vitro and in vivo, *Biomed. Mater.* 8 (2013), 035005.
- [25] B.K. Culpepper, M.C. Phipps, P.P. Bonvallet, S.L. Bellis, Enhancement of peptide coupling to hydroxyapatite and implant osseointegration through collagen mimetic peptide modified with a polyglutamate domain, *Biomaterials* 31 (2010) 9586–9594.
- [26] L. Kuang, J. Huang, Y. Liu, X. Li, Y. Yuan, C. Liu, Injectable hydrogel with NIR light-responsive, dual-mode PTH release for osteoregeneration in osteoporosis, *Adv. Funct. Mater.* 31 (2021), 2105383.
- [27] G. Guedes, S. Wang, F. Fontana, P. Figueiredo, J. Linden, A. Correia, R.J.B. Pinto, S. Hietala, F.L. Sousa, H.A. Santos, Dual-crosslinked dynamic hydrogel incorporating {Mo154} with pH and NIR responsiveness for chemo-photothermal therapy, *Adv. Mater.* (2021), e2007761.
- [28] D.L. Li, Q. Liu, Q.R. Qi, H. Shi, E.C. Hsu, W.Y. Chen, W.L. Yuan, Y.F. Wu, S.E. Lin, Y.T. Zeng, Z.Y. Xiao, L.Y. Xu, Y.R. Zhang, T. Stoyanova, W. Jia, Z. Cheng, Gold nanoclusters for NIR-II fluorescence imaging of bones, *Small* 16 (2020).
- [29] L. Tong, Q. Liao, Y. Zhao, H. Huang, A. Gao, W. Zhang, X. Gao, W. Wei, M. Guan, P. K. Chu, H. Wang, Near-infrared light control of bone regeneration with biodegradable photothermal osteoimplant, *Biomaterials* 193 (2019) 1–11.
- [30] D. Niu, Y. Li, J. Shi, Silica/organosilica cross-linked block copolymer micelles: a versatile theranostic platform, *Chem. Soc. Rev.* 46 (2017) 569–585.
- [31] S. Yang, D. Niu, N. Li, J. Gu, X. Dai, T. Yang, X. Gao, Y. Li, J. Shi, Block copolymer nanoparticle replicating strategy towards hierarchically mesoporous structured silica with predictable architectures, *Sci. Bull.* 66 (2021) 197–199.
- [32] L. Wang, W. Li, L. Yin, Y. Liu, H. Guo, J. Lai, Y. Han, G. Li, M. Li, J. Zhang, R. Vajtai, P.M. Ajayan, M. Wu, Full-color fluorescent carbon quantum dots, *Sci. Adv.* 6 (2020).
- [33] B. van Dam, H. Nie, B. Ju, E. Marino, J.M.J. Paulusse, P. Schall, M. Li, K. Dohnalova, Excitation-dependent photoluminescence from single-carbon dots, *Small* 13 (2017).
- [34] D. Li, L. Lin, Y. Fan, L. Liu, M. Shen, R. Wu, L. Du, X. Shi, Ultrasound-enhanced fluorescence imaging and chemotherapy of multidrug-resistant tumors using multifunctional dendrimer/carbon dot nanohybrids, *Bioact. Mater.* 6 (2021) 729–739.
- [35] G.A.M. Hutton, B.C.M. Martindale, E. Reisner, Carbon dots as photosensitisers for solar-driven catalysis, *Chem. Soc. Rev.* 46 (2017) 6111–6123.
- [36] J.B. Wu, M.L. Lin, X. Cong, H.N. Liu, P.H. Tan, Raman spectroscopy of graphene-based materials and its applications in related devices, *Chem. Soc. Rev.* 47 (2018) 1822–1873.
- [37] H. Wang, P. Gao, Y. Wang, J. Guo, K.-Q. Zhang, D. Du, X. Dai, G. Zou, Fluorescently tuned nitrogen-doped carbon dots from carbon source with different content of carboxyl groups, *Appl. Mater.* 3 (2015), 086102.
- [38] X.X. Gu, Y.X. Liu, G.P. Chen, H. Wang, C.M. Shao, Z.Y. Chen, P.H. Lu, Y.J. Zhao, Mesoporous colloidal photonic crystal particles for intelligent drug delivery, *ACS Appl. Mater. Interfaces* 10 (2018) 33936–33944.
- [39] S.R. Sershen, S.L. Westcott, J.L. West, N.J. Halas, An opto-mechanical nanoshell-polymer composite, *Appl. Phys. B* 73 (2001) 379–381.
- [40] W.-F. Lee, Y.-C. Yeh, Studies on preparation and properties of NIPAAm/hydrophobic monomer copolymeric hydrogels, *Eur. Polym. J.* 41 (2005) 2488–2495.
- [41] W.J. Chuang, W.Y. Chiu, Thermo-responsive nanofibers prepared from poly (N-isopropylacrylamide-co-N-methylol acrylamide), *Polymer* 53 (2012) 2829–2838.
- [42] Feil Herman, Bae You Han, Feijen Jan, S.W. Kim, Effect of comonomer hydrophilicity and ionization on the lower critical solution temperature of N-isopropylacrylamide copolymers, *Macromolecules* 26 (1993) 2496–2500.
- [43] T. Vermonden, R. Censi, W.E. Hennink, Hydrogels for protein delivery, *Chem. Rev.* 112 (2012) 2853–2888.
- [44] X. Zhang, D. Zeng, N. Li, J. Wen, X. Jiang, C. Liu, Y. Li, Functionalized mesoporous bioactive glass scaffolds for enhanced bone tissue regeneration *Sci., For. Rep.* 6 (2016).
- [45] C. Feng, W. Zhang, C. Deng, G. Li, J. Chang, Z. Zhang, X. Jiang, C. Wu, 3D printing of Lotus root-like biomimetic materials for cell delivery and tissue regeneration, *Adv. Sci.* 4 (2017), 1700401.
- [46] Y.C. Chiu, M.H. Cheng, H. Engel, S.W. Kao, J.C. Larson, S. Gupta, E.M. Brey, The role of pore size on vascularization and tissue remodeling in PEG hydrogels, *Biomaterials* 32 (2011) 6045–6051.
- [47] Y.J. Chai, D. Lin, Y.F. Ma, Y. Yuan, C.S. Liu, RhBMP-2 loaded MBG/PEGylated poly (glycerol sebacate) composite scaffolds for rapid bone regeneration, *J. Mater. Chem. B* 5 (2017) 4633–4647.
- [48] D. Lin, Y.J. Chai, Y.F. Ma, B. Duan, Y. Yuan, C.S. Liu, Rapid initiation of guided bone regeneration driven by spatiotemporal delivery of IL-8 and BMP-2 from hierarchical MBG-based scaffold, *Biomaterials* 196 (2019) 122–137.
- [49] M. Schumacher, P. Habibovic, S. van Rijt, Mesoporous bioactive glass composition effects on degradation and bioactivity, *Bioact. Mater.* 6 (2021) 1921–1931.
- [50] B. Sacchetti, A. Funari, S. Michienzi, S. Di Cesare, S. Piersanti, I. Saggio, E. Tagliafico, S. Ferrari, P.G. Robey, M. Riminucci, P. Bianco, Self-renewing osteoprogenitors in bone marrow sinusoids can organize a hematopoietic microenvironment, *Cell* 131 (2007) 324–336.
- [51] J. Zhang, Q. Zhao, L. Fu, S. Zheng, C. Wang, L. Han, Z. Gong, Z. Wang, H. Tang, Y. Zhang, CD301b(+) macrophages mediate angiogenesis of calcium phosphate bioceramics by CaN/NFATc1/VEGF axis, *Bioact. Mater.* 15 (2022) 446–455.
- [52] T. Kimura, C. Panaroni, E.B. Rankin, L.E. Purton, J.Y. Wu, Loss of parathyroid hormone receptor signaling in osteoprogenitors is associated with accumulation of multiple hematopoietic lineages in the bone marrow, *J. Bone Miner. Res.* 37 (2022) 1321–1334.
- [53] Y. Kang, T.A. Taton, Core/shell gold nanoparticles by self-assembly and crosslinking of micellar, block-copolymer shells, *Angew. Chem. Int. Ed.* 117 (2005) 413–416.
- [54] L.L. Hench, The story of Bioglass, *J. Mater. Sci. Mater. Med.* 17 (2006) 967–978.
- [55] X. Yan, C. Yu, X. Zhou, J. Tang, D. Zhao, Highly ordered mesoporous bioactive glasses with superior in vitro bone-forming bioactivities, *Angew. Chem., Int. Ed. Engl.* 43 (2004) 5980–5984.